Collimating Truncated Virtual Image Lens

Oskar Zetterstrom, *Graduate Student Member, IEEE*, Nelson J. G. Fonseca, *Senior Member, IEEE*, and Oscar Quevedo-Teruel, *Fellow, IEEE*

***Abstract*— The Luneburg lens is of significant interest for microwave and optical devices due to its wide-angle focusing properties. However, the inhomogeneous refractive index of the lens is restrictive and can be difficult to realize, especially at high frequency (typically millimeter-waves and above). Here, we present an inhomogeneous lens referred to as the collimating truncated virtual image lens, which is derived as a combination of the recently proposed virtual image lens and a conventional extended hemispherical lens. We investigate the operation of the proposed lens and we demonstrate that it provides similar focusing properties as the Luneburg lens, but with a flexible refractive index profile. This flexibility can be used to alleviate the strict manufacturing constraints typically associated with the Luneburg lens. We validate the properties of the proposed lens with a demonstrator at millimeter-wave frequencies showing that an antenna based on the proposed lens can obtain similar directivity and sidelobe levels to those obtained in an ideal Luneburg lens antenna, while the proposed lens is easier to realize. The collimating truncated virtual image lens is attractive for instruments and antennas at high frequency.**

***Index Terms*— Collimating lens, gradient refractive index lens, virtual image.**

I. Introduction

EMERGING communication and remote sensing applications are expected to operate at higher frequency than their predecessors to enable higher data rates and resolution. Specifically, the millimeter-wave frequency range is considered for terrestrial [1] and nonterrestrial [2] communication systems, and radar applications [3]. At these frequencies, high-gain antennas are used to overcome the significant free-space path loss. These high-gain antennas typically require beam-steering in order to provide sufficient angular coverage. Conventional beam-steering techniques using phased arrays can be prohibitive at high frequency due to the high cost of the necessary components. On the other hand, quasi-optical beam-forming technologies can be used to design cost-effective high-gain beam-steering antennas at high frequency [4].

Manuscript received 26 September 2023; revised 8 February 2024; accepted 29 February 2024. Date of publication 18 March 2024; date of current version 7 May 2024. This work was supported by ESA ARTES Advanced Technology under Contract 4000125905/18/NL. *(Corresponding author: Oskar Zetterstrom.)*

Oskar Zetterstrom and Oscar Quevedo-Teruel are with the Division of Electromagnetic Engineering and Fusion Science, KTH Royal Institute of Technology, 100 44 Stockholm, Sweden (e-mail: oskarz@kth.se; oscarqt@kth.se).

Nelson J. G. Fonseca was with Antenna and Sub-Millimetre Waves Section, European Space Agency, 2200 AG Noordwijk, The Netherlands. He is now with the Direction of Innovation, Anywaves, 31000 Toulouse, France.

Color versions of one or more figures in this article are available at https://doi.org/10.1109/TAP.2024.3376076.

Digital Object Identifier 10.1109/TAP.2024.3376076

In quasi-optical systems, a lens or reflector is used to shape the radiation from a feeding element. In reflectors and homogeneous lenses (i.e., lenses consisting of a homogeneous material), the shape of the beamformer dictates the focusing properties. To achieve a high gain, the feed is placed at the focal point of the beamformer and the radiation from the feed is collimated by the beamformer. The high-gain beam can be steered by moving the feeding element or by switching between multiple feeds placed along the focal arc of the beamformer. As such, costly components for beam-steering can be avoided. These conventional beamformers are subject to aberrations, which degrade their performance [5]. Spherical and comatic aberrations are the most common types, and in beamformers subject to these aberrations, the focusing properties vary within the aperture and under scanning conditions. As a result, antennas based on these beamformers suffer from reduced directivity, aperture efficiency, cross-polarization, and increased sidelobe levels [6] compared to antennas based on aberration-free beamformers. On the other hand, rotationally symmetric inhomogeneous lenses can be aberration-free. Importantly, the rotational symmetry suppresses the comatic aberrations, and consequently, the focusing properties are maintained when beam steering. Refractive index distributions that suppress the other types of aberration can be derived. As a result, devices based on these lenses can provide excellent characteristics, and this class of lenses is attractive for antenna applications at high frequency.

The first aberration-free refractive index distribution derived is attributed to Maxwell and is referred to as the Maxwell's fish-eye lens [7], [8]. This lens focuses the radiation of a feed to the antipodal point on the opposite side of the lens. The Maxwell's fish-eye lens can for instance be used to design waveguide crossings [9]. Luneburg later generalized the formulation so that the radiation from the source can be focused to a point any distance away from the lens [10]. The special case of Luneburg's formulation where the source is placed at the boarder of the lens and the focal point is placed at infinity is known as the Luneburg lens. This lens perfectly collimates the radiation from the source, and as a result, the Luneburg lens can be used to design antennas with a high directivity without degraded performance during beam scanning [11], [12]. Further generalizations of Maxwell's and Luneburg's formulations have been presented where the source and focus points can be inside the lens [13], [14], and these generalized Luneburg lenses have been used to design directive antennas [15], [16], [17]. Recently, the possibility of producing a virtual image on the same side of the lens as the source was demonstrated [18]. In a virtual image lens, the radiation

from the feed appears to be coming from the virtual image point instead of the source position and it was proposed to be integrated into the feeding system for reflector antennas.

At microwave frequencies, antennas based on Luneburg lenses are well documented [11], [12], [19], [20], [21], [22], [23] and have been proposed for remote sensing [24] and communication systems [6]. The inhomogeneous refractive index of the Luneburg lens has been mimicked in 2-D configurations by appropriately deforming a parallel plate waveguide. Such lenses are known as geodesic lenses and can be made fully metallic to provide high efficiency [25], [26], [27], [28], [29]. While this technique can be used to implement the continuous refractive index distribution without truncation and discretization errors, it is limited to 2-D configurations. Alternatively, the Luneburg lens can be implemented using layered concentric spherical or cylindrical shells [30], [31], however, this technique suffers from truncation and discretization effects and appropriate materials for each layer can be difficult and/or costly to find. Luneburg lenses based on quasi-periodic structures, where the inclusions are gradually varied throughout the lens, have been used to design planar [12], [23] and volumetric [19], [20], [21], [32] lens antennas. These lenses can be made fully metallic leading to a high efficiency [32], [33], [34]. Furthermore, additive manufacturing is an attractive option for the production of this type of lenses [19], [20], [21], suitable for mass production. However, quasi-periodic structures capable of mimicking the full refractive index range of the Luneburg lens can be difficult to implement. Additively manufactured lenses are often truncated at the boarder due to the difficulties in mimicking refractive indices close to unitary values as they require small (sub-wavelength) and fragile mechanical details. It is worth mentioning that, for increasingly higher frequencies, the realization of this type of Luneburg lenses is naturally more challenging due to the small wavelength and limited availability of bulk materials with the appropriate refractive index. A realization of a spherical Luneburg lens at infrared frequencies has been presented in recent years [35], albeit requiring high-precision micromachining of complex 3-D geometries. The difficulty in the realization of the lens at these frequencies has limited its use in optical and terahertz instruments.

We present a rotationally symmetric lens with spatially varying refractive index. Similar to the Luneburg lens, the proposed lens focuses impinging rays to the focal point located at the surface of the lens, and as a result, the proposed lens can be used to design antennas capable of wide-angle steering of a directive beam. Conversely to the Luneburg lens, the refractive index of the proposed lens can be tuned to facilitate the realization. The lens is derived co-locating a conventional hyper-hemispherical lens and a virtual image lens. We note that the proposed lens is a collimating lens, and is therefore different from the virtual image lens in [18], which is a diverging lens (except in the particular case of the Luneburg lens, found to be a common solution of the generalized Luneburg lens problem and its complementary formulation as defined in [18]). The aberrations in the proposed lens are inherited from the constituent lenses. Therefore, the proposed lens is subject to spherical aberrations, which results in somewhat reduced aperture efficiency and increased sidelobe levels compared to the Luneburg lens. However, we demonstrate that the performance degradation compared to the Luneburg lens is small for most practical cases of the proposed lens. Furthermore, the comatic aberrations are inherently suppressed by the rotational symmetry meaning that it can maintain its performance over wide-angle beam steering. The proposed lens is of interest for antennas and optical instruments where wide-angle focusing properties are needed.

The article is organized as follows. Section II presents the derivation of the collimating truncated virtual image lens. We also analyze the properties of the lenses with different refractive index distributions. In Section III, we present a practical implementation of the proposed lens at K_a-band and compare its properties to a Luneburg lens. Section IV presents the conclusions of this work.

II. Derivation of the Collimating Truncated Virtual Image Lens

In the quasi-optical limit, the propagation of electromagnetic waves is well described with rays, and the Eikonal equations of geometrical optics can be used to analyze the focusing properties of refractive index distributions [5]. The inverse problem, i.e., to synthesize a refractive index distribution given prescribed focusing properties, is more difficult. The theory of transformation optics provides one tool for such index synthesis [36], [37], but the obtained refractive index distribution is often anisotropic and/or contains regions with sub-unity or negative indices [38], [39]. As a result, transformation optics devices are typically difficult to realize, especially if a wide operational bandwidth is needed. However, by restricting the analysis to rotationally symmetric inhomogeneous media, solutions to the inverse problem with realizable material properties can be found in some cases. The approach proposed by Luneburg [10] exploits the conservation of the quantity $L = n(r)r\sin\alpha(r)$ along the ray paths in rotationally symmetric media [5], [40]. Here, $n(r)$ is the refractive index at the radial position r, and $\alpha(r)$ is the angle between the tangent to the ray path and the line connecting the origin and ray path at r. These quantities are illustrated in Fig. 1(a). L is referred to as the angular momentum of the ray as an analogy to the angular moment in classical mechanics. It is worth noting that rays traveling through the medium are at their smallest radial position when $\alpha = \pi/2$. We refer to this point as the turning point of the ray, denoted as $\tau = rn(r)$.

The differential change in the ray trajectory is geometrically related to $\alpha(r)$ as

$$r\frac{\mathrm{d}\varphi}{\mathrm{d}r} = \tan\alpha(r) \tag{1}$$

which can be expressed in terms of L

$$r\frac{\mathrm{d}\varphi}{\mathrm{d}r} = \frac{L}{\sqrt{\tau^2(r) - L^2}}. \tag{2}$$

Equation (2) is conveniently rearranged as

$$\mathrm{d}\varphi = \frac{L\mathrm{d}r}{r\sqrt{\tau^2(r) - L^2}} \tag{3}$$

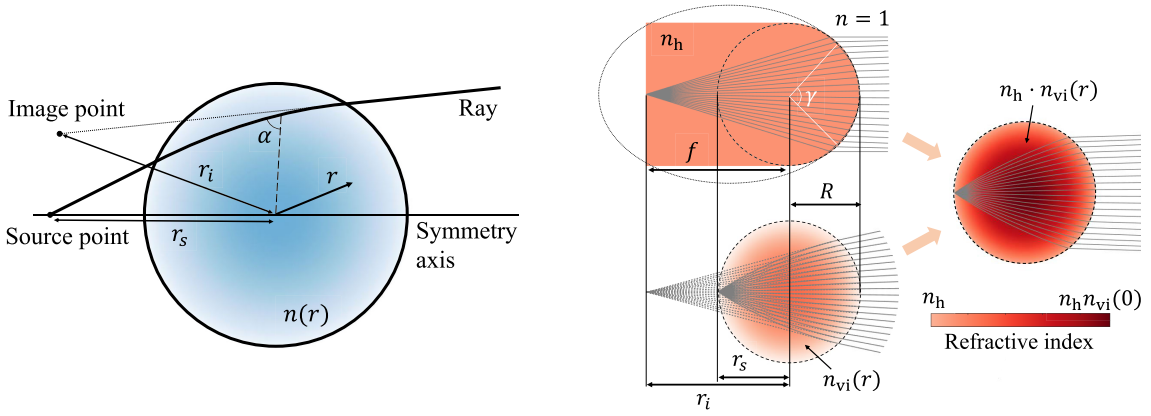

(a) (b)

Fig. 1. Problem definition and important quantities. (a) Schematic representation of the operation of the diverging virtual image lens. The outline of the inhomogeneous part is indicated with solid black circle. (b) Ray tracing representation of the extended hemispherical lens, the diverging virtual image lens, and the proposed collimating truncated virtual image lens. The collimation in the proposed lens is obtained by collocating the image position of the diverging virtual image lens with the focal point of the extended hemispherical lens.

to allow for integration between the source and image radial positions to retrieve the total angular change of a ray when propagating through the medium [10], [18], [40]. The contribution from the inhomogeneous region of the media to the change in the ray's trajectory is often referred to as the scattering angle. The scattering angle depends on the problem formulation, but of importance in this work is the scattering angle defined in [18]

$$\chi(L) = M\pi + \arcsin\frac{L}{r_s} - \arcsin\frac{L}{r_i}. \tag{4}$$

Here M is the turning angle describing the total change of a ray's polar angle (M is a nonnegative real number), and r_s is the radial position of the source. The scattering angle in (4) corresponds to the virtual image lens, and the virtual image is created at the radial position r_i, as illustrated in Fig. 1. The refractive index for a medium with the scattering angle (4) can be found as [18]

$$n = \exp\left(\frac{1}{\pi}\int_{\tau}^{1}\frac{\chi(t)}{\sqrt{t^2-\tau^2}}\mathrm{d}t\right). \tag{5}$$

Here, the refractive index of the inhomogeneous media is normalized to the surrounding homogeneous medium, and the radius of the inhomogeneous medium is normalized to 1 without lack of generality.

In a lens defined by (4), rays from the point source appear to an observer at the opposite side of the lens as if they come from the point image. This property of the virtual image lens is obtained only if the surrounding homogeneous medium extends to infinity. On the other hand, if the medium is truncated, i.e., the refractive index at the surface of the lens is not equal to the surrounding homogeneous refractive index, the rays refract at the truncation, and with an appropriate design of the truncation, the rays can be perfectly collimated. In fact, perfect collimation of the rays is obtained for an elliptical truncation having the image point of the virtual image lens collocated with the far focal point of the ellipse. Note that for perfect collimation, the homogeneous refractive index of this lens must be the inverse of the eccentricity e of the ellipse: $n_h = 1/e = a/\sqrt{a^2-b^2}$, where a and b are the major and minor axes of the ellipse. An elliptical truncation disrupts the rotational symmetry of the device, meaning that comatic aberrations are observed in such a medium. On the other hand, if the truncation is spherical and concentric to the inhomogeneous medium, the rotational symmetry of the device is preserved, but the focusing is subject to spherical aberrations. Fig. 1(b) presents the ray paths from a point source in an extended hemispherical lens, in a virtual image lens, and in the proposed lens that is obtained as the combination of the two other lenses. In this illustrative example, we have used $r_s = R$, $r_i = f = 2R$, and $n_h = 1.37$. R is the radius of the lens and it is found by least-square fitting a circle to the ellipse with $e = 1/n_h = 0.73$ within the angular range $\gamma \leq \pi/2$ [defined in Fig. 1(b)]. It is important to note that all radial positions have been normalized to R in the calculations of the refractive index using (4) and (5). The proposed lens produces rays that are quasi-parallel at the output when it is excited by a point source on the surface of the lens. The properties of the lens are naturally reciprocal, and the lens focuses incident parallel rays to a small region on the surface of the lens.

The collimation of the rays from a point source on the surface of the lens can be obtained for different n_h, as exemplified in Fig. 2. Fig. 2(a) presents the radial refractive index profiles for different n_h, with the Luneburg lens profile corresponding to $n_h = 1$. It is interesting to note that the relative range of the required refractive index decreases with increasing n_h, which can alleviate the realization of the lens, in particular, if it is done by patterning a bulk material, as in [35]. The reason for the reduced refractive index range in lenses with higher n_h is the increased refraction at the lens' surface, which helps collimating the rays. The spherical aberrations in the proposed lens depend on how well the spherical truncation approximates the perfectly collimating elliptical truncation, meaning that the spherical aberrations depend on n_h. The approximation of the ellipse with the spherical lens is illustrated in Fig. 2(b)–(e). The eccentricity of the ellipses is indicated in the figures, and

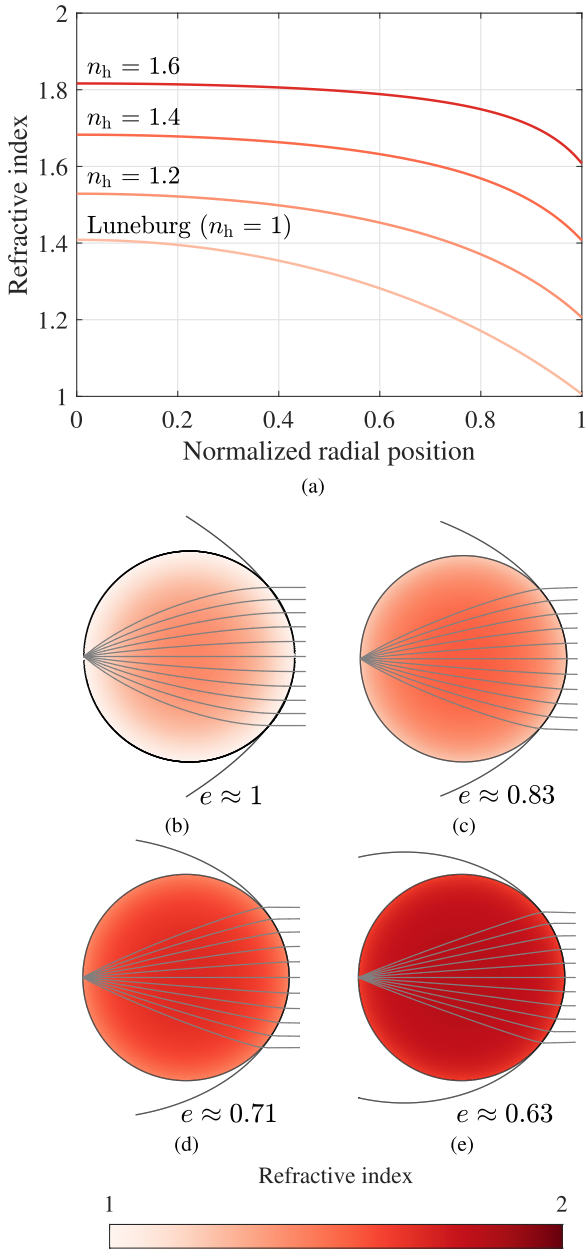

Fig. 2. Collimating truncated virtual image lenses with different refractive index profiles. (a) Refractive index profiles for different n_h. The Luneburg lens profile is obtained when $n_h = 1$. (b)–(e) Illustration of the approximation of the elliptical outline with the spherical lens for truncated collimating virtual image lenses with $n_h = 1$, $n_h = 1.2$, $n_h = 1.4$, and $n_h = 1.6$. The eccentricity of the ellipse is indicated in the figures and is obtained as $e = 1/n_h$. The ray paths through the lenses are indicated with gray lines.

is obtained as $e = 1/n_h$. The accuracy of this approximation is increasing with n_h, but even for small n_h, the extended hemisphere can approximate an ellipse well in the central part of the aperture, which typically concentrates most of the emitted power in the case of practical sources with tapered patterns such as open-ended waveguides and horn antennas. Fig. 3 presents the ray paths in a collimating virtual image lens with $n_h = 1.4$ for different source positions along the lens boarder. The rotational symmetry of the lens ensures that the focusing properties are maintained for any direction, which is

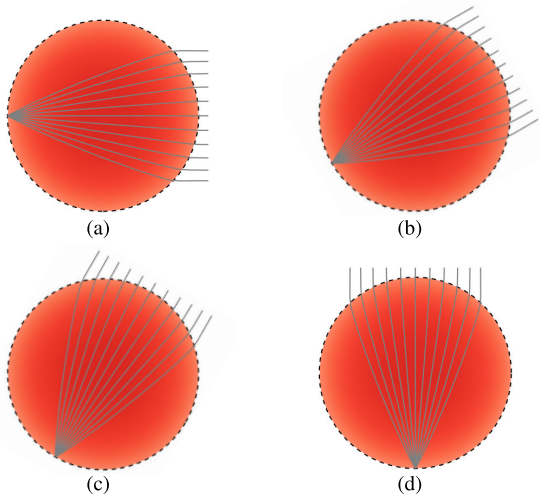

Fig. 3. Ray-tracing simulation of the proposed lens ($n_h = 1.4$) with source positions at the reference position (a) and displaced 30° (b), 60° (c), and 90° (d).

attractive for antenna applications requiring wide angle beam steering.

Fig. 4(a) presents the directivity at 30 GHz for lenses with different n_h when excited by a square waveguide at the focal point. The waveguide width is 0.8λ and the lens radius is $R = 4\lambda$. The inset shows the 3-D radiation pattern for the cases $n_h = 1$, $n_h = 1.3$, and $n_h = 1.6$. The lenses are implemented assuming dielectric materials ($\mu_r = 1$), and as a result, reflections occur at the termination of the lens for $n_h \geq 1$. These reflections result in reduced directivity for large n_h, but for moderate n_h, the focusing properties of the Luneburg lens are maintained. It is worth noting that the reflections can be mitigated using an anti-reflection coating, although this is not expected to be necessary for most practical realizations of the proposed lens. On the other hand, most materials used for the realization of such inhomogeneous lenses have refractive indices of $n \lesssim 1.7$. For example, the bulk materials in [35] and [15] have refractive indices $n = 1.52$ and $n = 1.73$. This means that the maximum realizable refractive index using common bulk materials is less than approximately 1.7, which means that n_h can be typically smaller than 1.4.

Fig. 4(b)–(e) presents the simulated electric field distribution for lenses with the refractive index distributions in Fig. 2(a). The lenses are excited by a point source at the left side of the lens and the radius of the lenses is $R = 4\lambda$. The resulting wavefronts observed at the right side of the lenses are characteristic of plane waves, which demonstrates the focusing properties of the lenses with different n_h. The reflections at the lens termination for $n_h > 1$ produces a standing wave pattern at the aperture around the lens contour. Additionally, in the lens with $n_h = 1.6$, we observe a standing wave pattern along the surface of the lens. This standing wave is caused by the reflection of the rays/waves with a high angle of incidence to the lens' surface. In fact, for large n_h, rays with large angular momentum may be incident on the lens' surface at angles larger than the critical angle and are therefore confined in the lens until dissipated.

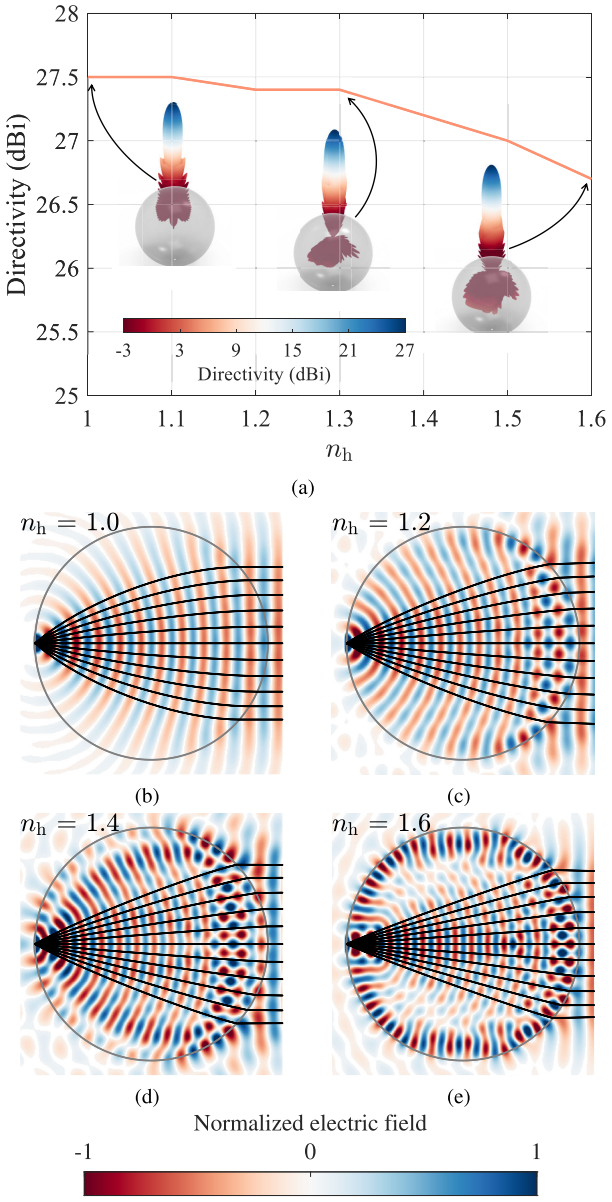

Fig. 4. Focusing properties of collimating truncated virtual image lenses with different refractive index profiles. (a) Simulated directivity at 30 GHz for collimating truncated virtual image lenses with different refractive index profiles. The insets display the 3-D radiation pattern for the cases $n_h = 1$ (Luneburg lens), $n_h = 1.3$, and $n_h = 1.6$. The gray spheres represent the lenses, and they have a radius of $R = 40$ mm. The lenses are excited by an 8 mm wide square waveguide aperture. (b)–(e) Normalized electric field distribution at 30 GHz in lenses with $n_h = 1$, $n_h = 1.2$, $n_h = 1.4$, and $n_h = 1.6$. The ray paths through the lenses are indicated with the black lines.

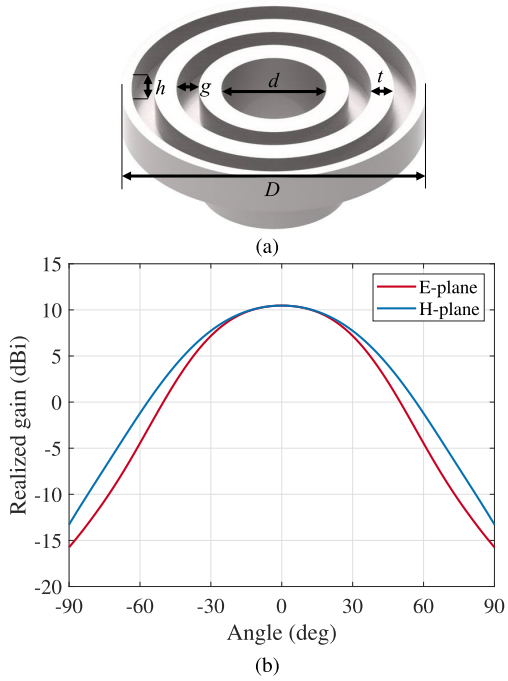

Fig. 5. Feeding element for the two lenses. (a) Illustration of the feed with dimensions highlighted. (b) Realized gain in the E- and H-planes at 30 GHz for the isolated feed. The dimensions are: $d = 8.9$ mm, $D = 25.9$ mm, $t = 1.9$ mm, $g = 1.9$ mm, and $h = 2.4$ mm.

III. Demonstration at K_a-Band

We demonstrate the operation of the proposed lens with a prototype at K_a-band. To better illustrate the properties of the proposed lens, we compare it to a conventional Luneburg lens. The two lenses are fed by an open-ended circular waveguide. Corrugations are placed around the waveguide aperture to reduce the diffraction effects. The feed element and its simulated radiation pattern are presented in Fig. 5. The dimensions are: $d = 8.9$ mm, $D = 25.9$ mm, $t = 1.9$ mm, $g = 1.9$ mm, and $h = 2.4$ mm. The two lenses are realized using fused filament additive manufacturing (abbreviated as FDM), and the inhomogeneous refractive indices are mimicked using a quasi-periodic structure similar to the one in [15]. Specifically, the quasi-periodic inclusions are arranged in a simple cubic lattice and are cubic air cavities of width w in a bulk medium with the refractive index $n_b = 1.61$. The spatial periodicity of the structure is p. The unit cell of the structure and the corresponding irreducible Brillouin zone are illustrated in Fig. 6(a). Fig. 6(b) presents the effective refractive index as a function of frequency for different cavity sizes. The response of the structure is investigated along the three edges of the irreducible Brillouin zone. The period is $p = 2.5$ mm. It is worth noting that while the lens is derived based on geometrical optics and is therefore frequency-independent by design, the implementation reported here using a quasi-periodic structure imposes a bandwidth limitation. With the structure in Fig. 6, the lens is expected to operate at frequencies up to at least 30 GHz, after which the response along the three reported directions is different (indicating anisotropy) and the refractive index diverges. The realizable effective refractive index range is dictated by the manufacturing, and in the case of FDM, the lowest realizable effective refractive index is limited by the extrusion width. In our case, the extrusion width is 0.4 mm, which means that effective refractive indices below 1.25 cannot be produced as this effective index corresponds to a wall width of 0.4 mm. As a result, we set $n_h = 1.25$ in our design. Fig. 6(c) presents the refractive index distribution for the proposed collimating truncated virtual image lens and the reference Luneburg lens. The realizable range of refractive indices is indicated, and we see that approximately 30% of the Luneburg lens refractive index cannot be realized with the chosen manufacturing

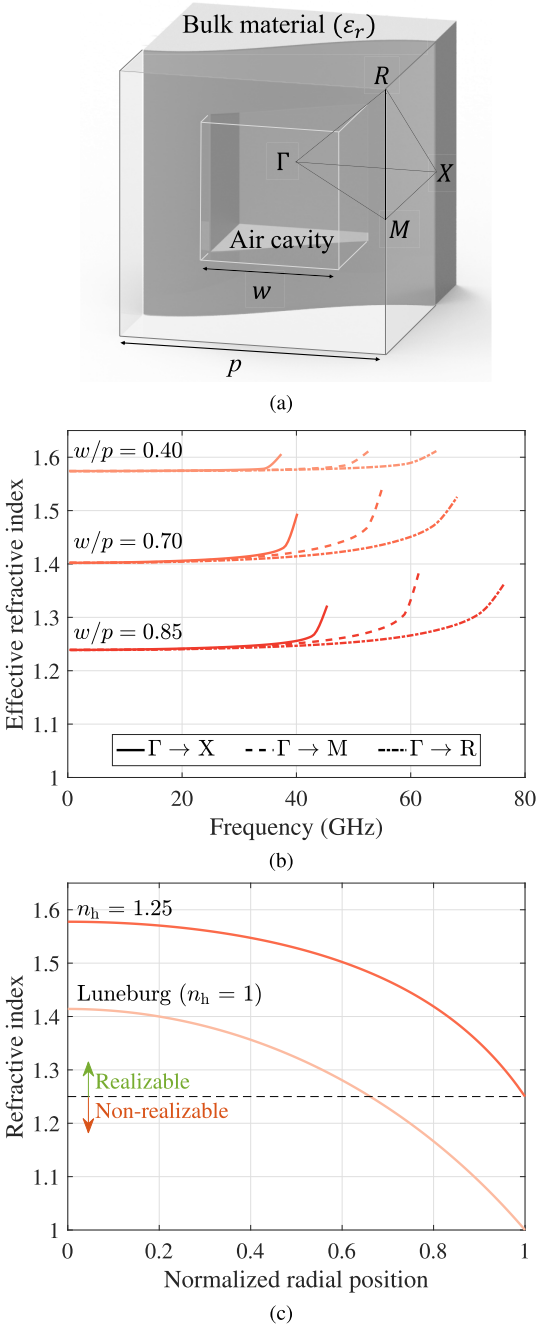

Fig. 6. Implementation of the lens' refractive index. (a) Geometry of the unit cell used in the lens design. Periodic boundary conditions are applied in all directions. (b) Effective refractive index for different sizes of the air cavity. The period is $p = 2.5$ mm, and the response is investigated along the edges of the irreducible Brillouin zone. (c) Refractive index profiles of the proposed collimating truncated virtual image lens and the reference Luneburg lens. The realizable range of indices is indicated.

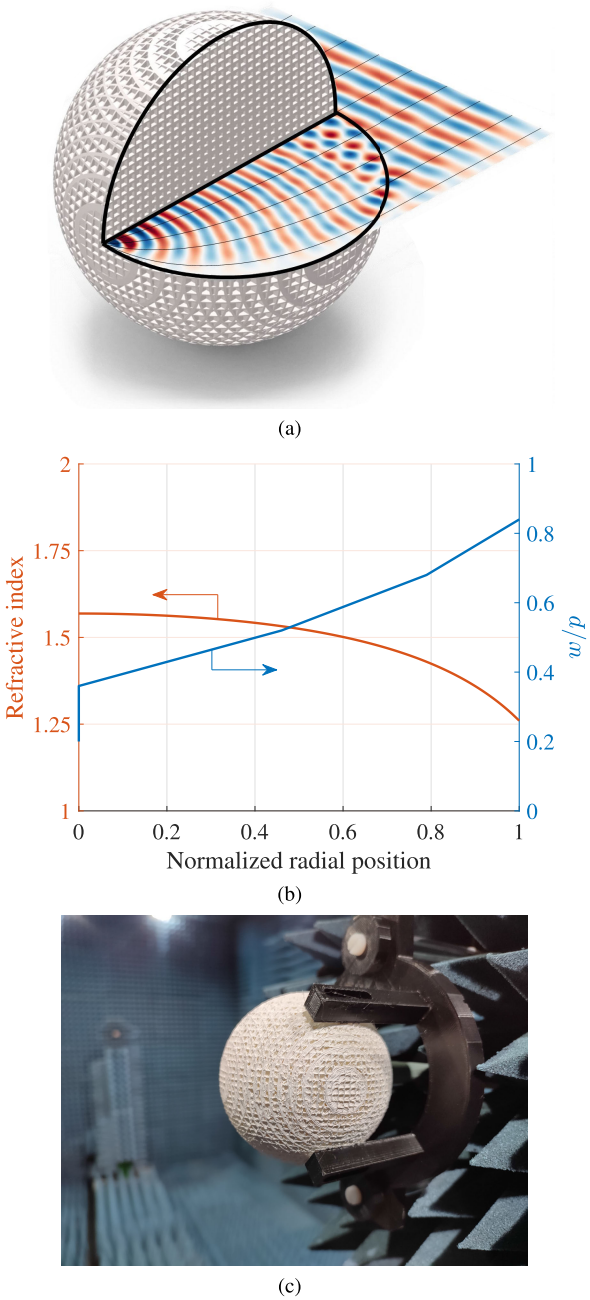

Fig. 7. Realization of the collimating virtual image lens. (a) Three-dimensional model of the lens. The electric field is obtained at 30 GHz. (b) Radial map of the refractive index and corresponding air cavity size ($p = 2.5$ mm). (c) Photograph of the lens prototype mounted in the anechoic chamber used for the experimental verification.

technique. On the other hand, the refractive index of the proposed lens can be realized with the chosen manufacturing technique. While the refractive index of the Luneburg lens may be realizable with alternative manufacturing techniques at millimeter-wave frequencies, as exemplified in [20] and [21], it is important to note that such techniques are often expensive. Furthermore, any additive manufacturing technique is limited by the smallest realizable dimension and as a result would require a truncation of the Luneburg refractive index at a sufficiently high frequency. The proposed lens can be used to alleviate these limitations.

Fig. 7 presents the lens design and prototype. The refractive index of the proposed lens is mimicked by varying the cavity width from $0.4p$ to $0.85p$ ($p = 2.5$ mm) and the lens radius is 4 cm. A Luneburg lens is also manufactured for comparison. In the reference lens, the diameter is rescaled so that the radius of the realizable part of the refractive index distribution is 4 cm. This is done to ensure that the aperture size is the same for the proposed and the reference Luneburg lenses, thus enabling a fair comparison. Fig. 8 presents the

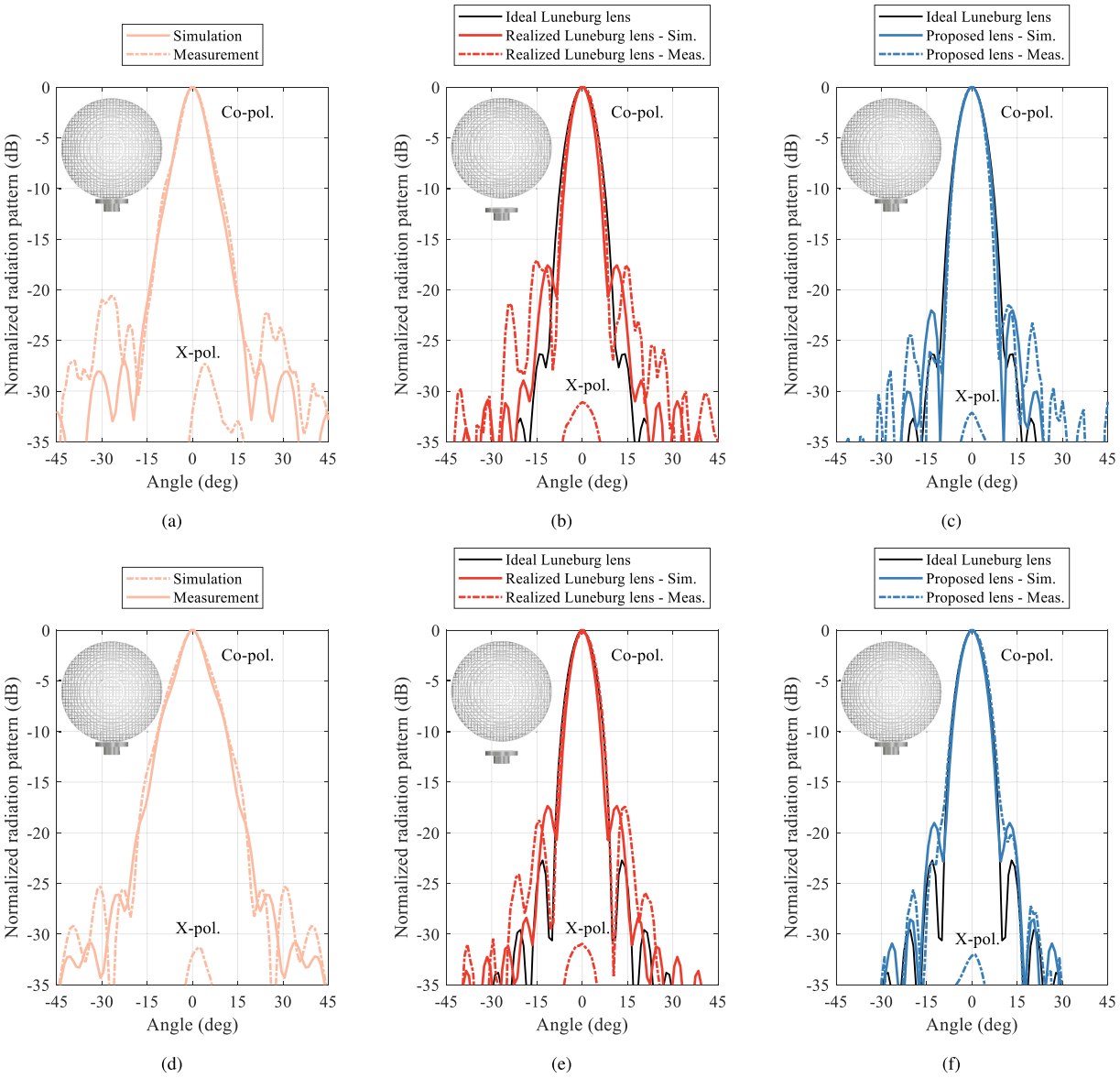

Fig. 8. Normalized radiation pattern at 30 GHz of the lenses when excited by a circular waveguide: (a)–(c) H-plane and (d)–(f) E-plane. Simulated and measured radiation pattern for (a) and (d) Luneburg lens with the feed at the surface of the lens, (b) and (e) Luneburg lens with the feed moved away 0.8 cm from the surface of the lens (as indicated in the inset) to recover the focusing properties, and (c) and (f) proposed collimating virtual image lens with the feed at the surface of the lens. The results in (b), (c), (e), and (f) are compared to simulations of an ideal Luneburg lens.

normalized radiation pattern for the Luneburg and proposed lens antennas at 30 GHz. Fig. 8(a) and (c) presents the H- and E-plane radiation patterns of the Luneburg lens antenna excited by the waveguide placed at the lens' surface. Since only part of the refractive index range of the Luneburg lens is realized, the observed radiation pattern is distorted. In fact, the waveguide excitation is not placed at the focus of the lens, and by displacing the waveguide excitation from the lens' surface, the radiation properties of the lens antenna system may be improved, as illustrated in Fig. 8(b) (H-plane) and Fig. 8(d) (E-plane). Here, the feed is displaced 0.8 cm ($0.2R$) from the lens surface, and we observe that the radiation pattern is somewhat restored, albeit exhibiting high side lobes and slightly smaller beamwidth compared to the case with an ideal Luneburg lens (black line in the figures). The radiation pattern of the collimating virtual image lens antenna excited by the waveguide placed at the lens' surface is presented in Fig. 8(c) (H-plane) and Fig. 8(f) (E-plane). We observe that the proposed lens provides focusing properties similar to those of the ideal Luneburg lens. Importantly, the beamwidth and sidelobe levels obtained with the proposed lens are comparable to those obtained with the ideal Luneburg lens. The slightly higher side lobes in the proposed lens compared to the ideal Luneburg lens are attributed to spherical aberrations. We also note that the radiation performance of the proposed lens antenna is stable for different beam directions due to the angularly stable response of the quasi-periodic structure for frequencies below 30 GHz.

The operating bandwidth of the antenna is restricted in the upper end by the dispersion of the quasi-periodic structure (30 GHz), and in the lower end by the cut-off frequency of the feeding element, providing an acceptable return loss above 26 GHz. Fig. 9 presents the simulated and measured reflection coefficient for the feed and lens system

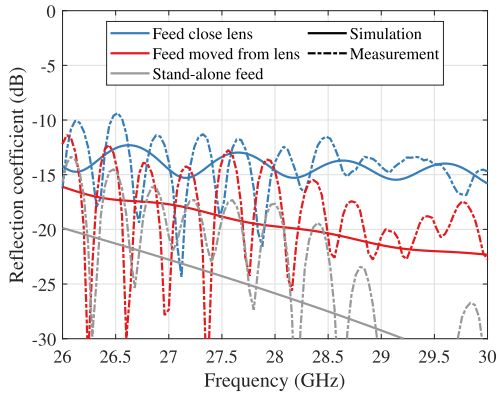

Fig. 9. Simulated and measured reflection coefficients for the isolated feed and for the feed and lens system in two configurations (feed aperture at the lens surface and moved 8 mm away from the lens surface).

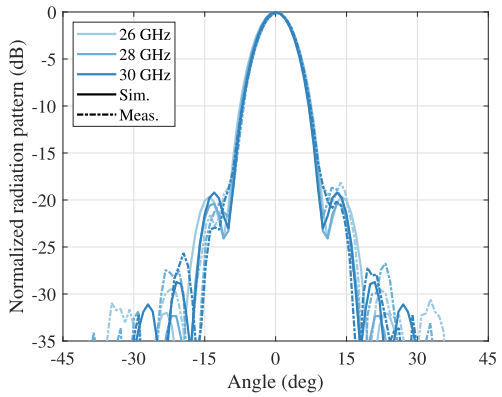

Fig. 10. Simulated and measured normalized radiation pattern in the E-plane of the proposed lens antennas.

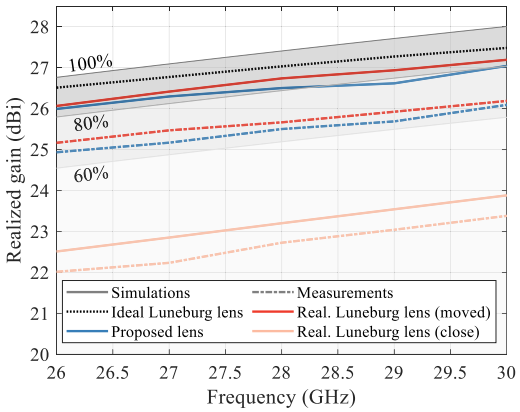

Fig. 11. Simulated and measured realized gain of the Luneburg and proposed lens antennas. The simulated performance of an antenna with an ideal Luneburg lens is included for reference and the expected directivity with aperture efficiencies of 60%, 80%, and 100% are indicated.

from 26 to 30 GHz. The presented reflection coefficients correspond to the isolated feed, and for the feed and lens system in two configurations (with the feed at the lens' surface and with the feed displaced 0.8 cm). The feed is designed assuming that it is isolated, and the reflection coefficient increases with the feed placed close to the lens, but it remains below -10 dB. We note that the lens' impedance can be accounted for in the design of the feed to reduce the reflections, but it is considered to be out of the scope of this work. Fig. 10 presents the simulated and measured E-plane normalized radiation patterns

TABLE I
COMPARISON OF DIFFERENT WIDE SCANNING COLLIMATING LENSES FOR ANTENNA APPLICATIONS

Ref.	[19]	[20]	[21]	This work
Lens	Luneburg lens	Luneburg lens	Luneburg lens	Collimating truncated virtual image lens
Realized index range	1-1.4	≈1.1-1.4	≈1.1-1.4	1.25-1.6
Upper frequency	20 GHz	110 GHz	38 GHz	30 GHz
Manufacturing complexity	High	High	High	Low
Index truncated	No	Yes	Yes	No
Manufacturing technique	Polymer jetting	High-accuracy FDM	ND*	Low-cost FDM
Comment	Steering not supported	Anisotropic implementation	Anisotropic implementation	Isotropic implementation
*ND	Not disclosed			

of the proposed lens at 26, 28, and 30 GHz. The simulations and measurements are in good agreement, and the sidelobe level and beamwidth are stable over the considered bandwidth. The simulated and measured realized gain of the lens antennas are compared in Fig. 11. The measured gain is obtained by comparing the power received at the probe when using the proposed lens antenna with the power received using a reference antenna with known calibrated gain. The simulated realized gain achieved with the collimating truncated virtual image lens is similar to that of the ideal Luneburg lens antenna, and the approximately 0.5 dB lower gain in the proposed lens is attributed to the spherical aberrations and dielectric losses. We note that $\tan\delta = 0.001$ is assumed in the simulations of the proposed lens while the ideal Luneburg lens antenna is assumed to be lossless. The measured gain is roughly 1 dB lower than the simulated value. This difference is attributed to larger dielectric losses in the measurements than those assumed in the simulations.

Table I compares the proposed lens concept to alternative additively manufactured wide scanning collimating gradient index lens solutions in the literature [19], [20], [21]. Notably, while successful demonstrations of Luneburg lenses exist up to 110 GHz, these lenses require expensive manufacturing techniques to be realized. Furthermore, the effective medium of the lenses presented in [20] and [21] is anisotropic which impacts the scanning performance. On the other hand, the proposed lens concept can be used to alleviate the manufacturing constraints of wide scanning collimating lenses, in particular by allowing for the realization of cost-effective isotropic effective media.

IV. CONCLUSION

We proposed a rotationally symmetric inhomogeneous lens that collimates rays from a point on the lens' surface to quasi-parallel rays at the diametrically opposite side of the lens. Due to the rotational symmetry, the proposed lens maintains its focusing properties for all angles of incidence. The lens is derived by combining the properties of a virtual

image lens with an extended hemispherical lens, and it is referred to as the collimating truncated virtual image lens. We demonstrate that the focusing properties of the proposed lens are similar to those of the Luneburg lens. However, conversely to the Luneburg lens, the refractive index distribution of the proposed lens can be tuned to simplify the realization. To validate the analysis and highlight the importance of the work, we manufactured and tested two lens antennas; one based on the Luneburg lens and one based on the proposed lens. In this comparison, we highlight that the antenna based on the collimating truncated virtual image lens provides similar gain and sidelobe level performance as an antenna based on an ideal Luneburg lens. On the other hand, the manufactured Luneburg lens suffers from reduced focusing properties compared to the ideal case due to the difficulties in manufacturing. Robust manufacturing is of significant importance at high frequency (typically millimeter-wave frequencies and higher), where the difficulty of realization has limited the use of Luneburg lenses, despite their attractive properties. As such, the proposed lens is expected to facilitate the development of advanced quasi-optical systems at microwave, terahertz, and optical frequencies.

REFERENCES

[1] *Ericsson AB*. Sep. 22, 2023. [Online]. Available: https://www.ericsson.com/en/reports-and-papers/further-insights/leveraging-the-potential-of-5g-millimeter-wave

[2] G. Amendola et al., "Low-Earth orbit user segment in the Ku and Ka-band: An overview of antennas and RF front-end technologies," *IEEE Microw. Mag.*, vol. 24, no. 2, pp. 32–48, Feb. 2023.

[3] A. Al-Hourani et al., "Millimeter-wave integrated radar systems and techniques," in *Academic Press Library in Signal Processing*, vol. 7. New York, NY, USA: Academic, 2018, pp. 317–363.

[4] Y. J. Guo, M. Ansari, R. W. Ziolkowski, and N. J. G. Fonseca, "Quasi-optical multi-beam antenna technologies for B5G and 6G mmWave and THz networks: A review," *IEEE Open J. Antennas Propag.*, vol. 2, pp. 807–830, 2021.

[5] M. Born and E. Wolf, *Principles of Optics*. Cambridge, U.K.: Cambridge Univ. Press, 1999.

[6] O. Quevedo-Teruel, M. Ebrahimpouri, and F. Ghasemifard, "Lens antennas for 5G communications systems," *IEEE Commun. Mag.*, vol. 56, no. 7, pp. 36–41, Jul. 2018.

[7] J. C. Maxwell, "Problems," *Camb. Dublin Math. J.*, vol. 8, p. 188, 1853.

[8] J. C. Maxwell, "Solutions to problems," *Cambridge Dublin Math. J.*, vol. 9, pp. 9–11, 1854.

[9] S. H. Badri, M. M. Gilarlue, and H. Taghipour-Farshi, "Rectangular Maxwell's fisheye lens via transformation optics as a crossing medium for dissimilar waveguides," *J. Opt. Soc. Amer. B, Opt. Phys.*, vol. 37, no. 8, pp. 2437–2443, Aug. 2020.

[10] R. K. Luneburg, *Mathematical Theory of Optics*. Providence, RI, USA: Brown Univ. Press, 1944.

[11] G. Peeler and D. Archer, "A two-dimensional microwave Luneberg lens," *Trans. IRE Prof. Group Antennas Propag.*, vol. 1, no. 1, pp. 12–23, Jul. 1953.

[12] C. Pfeiffer and A. Grbic, "A printed, broadband Luneburg lens antenna," *IEEE Trans. Antennas Propag.*, vol. 58, no. 9, pp. 3055–3059, Sep. 2010.

[13] A. S. Gutman, "Modified Luneberg lens," *J. Appl. Phys.*, vol. 25, no. 7, pp. 855–859, Jul. 1954.

[14] S. P. Morgan, "General solution of the Luneberg lens problem," *J. Appl. Phys.*, vol. 29, no. 9, pp. 1358–1368, Sep. 1958.

[15] O. Bjorkqvist, O. Zetterstrom, and O. Quevedo-Teruel, "Additive manufactured dielectric Gutman lens," *Electron. Lett.*, vol. 55, no. 25, pp. 1318–1320, Dec. 2019.

[16] P. Bantavis, C. G. Gonzalez, R. Sauleau, G. Goussetis, S. Tubau, and H. Legay, "Broadband graded index Gutman lens with a wide field of view utilizing artificial dielectrics: A design methodology," *Opt. Exp.*, vol. 28, no. 10, pp. 14648–14661, May 2020.

[17] O. Zetterstrom et al., "V-band geodesic generalized Luneburg lens antenna with high beam crossover gain," *IEEE Trans. Antennas Propag.*, vol. 71, no. 9, pp. 7591–7596, Sep. 2023.

[18] N. J. G. Fonseca, T. Tyc, and O. Quevedo-Teruel, "A solution to the complement of the generalized Luneburg lens problem," *Commun. Phys.*, vol. 4, no. 1, p. 270, 2021.

[19] M. Liang, W. Ng, K. Chang, K. Gbele, M. E. Gehm, and H. Xin, "A 3-D Luneburg lens antenna fabricated by polymer jetting rapid prototyping," *IEEE Trans. Antennas Propag.*, vol. 62, no. 4, pp. 1799–1807, Apr. 2014.

[20] Z. Larimore, S. Jensen, A. Good, A. Lu, J. Suarez, and M. Mirotznik, "Additive manufacturing of Luneburg lens antennas using space-filling curves and fused filament fabrication," *IEEE Trans. Antennas Propag.*, vol. 66, no. 6, pp. 2818–2827, Jun. 2018.

[21] Y. Li, L. Ge, M. Chen, Z. Zhang, Z. Li, and J. Wang, "Multibeam 3-D-printed Luneburg lens fed by magnetoelectric dipole antennas for millimeter-wave MIMO applications," *IEEE Trans. Antennas Propag.*, vol. 67, no. 5, pp. 2923–2933, May 2019.

[22] F. Fan, M. Cai, J. Zhang, Z. Yan, and J. Wu, "Wideband low-profile Luneburg lens based on a glide-symmetric metasurface," *IEEE Access*, vol. 8, pp. 85698–85705, 2020.

[23] O. Zetterstrom, R. Hamarneh, and O. Quevedo-Teruel, "Experimental validation of a metasurface Luneburg lens antenna implemented with glide-symmetric substrate-integrated holes," *IEEE Antennas Wireless Propag. Lett.*, vol. 20, pp. 698–702, 2021.

[24] L. Xue and V. F. Fusco, "24 GHz automotive radar planar Luneburg lens," *IET Microw., Antennas Propag.*, vol. 1, pp. 624–628, Jun. 2007.

[25] R. F. Rinehart, "A solution of the problem of rapid scanning for radar antennae," *J. Appl. Phys.*, vol. 19, no. 9, pp. 860–862, Sep. 1948.

[26] R. F. Rinehart, "A family of designs for rapid scanning radar antennas," *Proc. IRE*, vol. 40, no. 6, pp. 686–688, Jun. 1952.

[27] K. S. Kunz, "Propagation of microwaves between a parallel pair of doubly curved conducting surfaces," *J. Appl. Phys.*, vol. 25, no. 5, pp. 642–653, May 1954.

[28] N. J. G. Fonseca, Q. Liao, and O. Quevedo-Teruel, "Equivalent planar lens ray-tracing model to design modulated geodesic lenses using non-Euclidean transformation optics," *IEEE Trans. Antennas Propag.*, vol. 68, no. 5, pp. 3410–3422, May 2020.

[29] O. Quevedo-Teruel et al., "Geodesic lens antennas for 5G and beyond," *IEEE Commun. Mag.*, vol. 60, no. 1, pp. 40–45, Jan. 2022.

[30] J. R. Sanford, "Scattering by spherically stratified microwave lens antennas," *IEEE Trans. Antennas Propag.*, vol. 42, no. 5, pp. 690–698, May 1994.

[31] J. Bor, O. Lafond, H. Merlet, P. Le Bars, and M. Himdi, "Foam based Luneburg lens antenna at 60 GHz," *Prog. Electromagn. Res. Lett.*, vol. 44, pp. 1–7, 2013.

[32] M. Ansari, B. Jones, and Y. J. Guo, "Spherical Luneburg lens of layered structure with low anisotropy and low cost," *IEEE Trans. Antennas Propag.*, vol. 70, no. 6, pp. 4307–4318, Jun. 2022.

[33] O. Quevedo-Teruel, J. Miao, M. Mattsson, A. Algaba-Brazalez, M. Johansson, and L. Manholm, "Glide-symmetric fully metallic Luneburg lens for 5G communications at Ka-band," *IEEE Antennas Wireless Propag. Lett.*, vol. 17, no. 9, pp. 1588–1592, Sep. 2018.

[34] H. Lu, Z. Liu, Y. Liu, H. Ni, and X. Lv, "Compact air-filled Luneburg lens antennas based on almost-parallel plate waveguide loaded with equal-sized metallic posts," *IEEE Trans. Antennas Propag.*, vol. 67, no. 11, pp. 6829–6838, Nov. 2019.

[35] Y.-Y. Zhao, Y.-L. Zhang, M.-L. Zheng, X.-Z. Dong, X.-M. Duan, and Z.-S. Zhao, "Three-dimensional Luneburg lens at optical frequencies," *Laser Photon. Rev.*, vol. 10, no. 4, pp. 665–672, 2016.

[36] U. Leonhardt, "Optical conformal mapping," *Science*, vol. 312, no. no. 5781, pp. 1777–1780, Apr. 2006.

[37] J. B. Pendry, D. Schurig, and D. R. Smith, "Controlling electromagnetic fields," *Science*, vol. 312, no. no. 5781, pp. 1780–1782, Jun. 2006.

[38] N. Kundtz and D. R. Smith, "Extreme-angle broadband metamaterial lens," *Nature Mater.*, vol. 9, no. 2, pp. 129–132, Feb. 2010.

[39] R. Liu, C. Ji, J. J. Mock, J. Y. Chin, T. J. Cui, and D. R. Smith, "Broadband ground-plane cloak," *Science*, vol. 323, no. 5912, pp. 366–369, Jan. 2009.

[40] T. Tyc, L. Herzánová, M. Šarbort, and K. Bering, "Absolute instruments and perfect imaging in geometrical optics," *New J. Phys.*, vol. 13, no. 11, Nov. 2011, Art. no. 115004.

Oskar Zetterstrom (Graduate Student Member, IEEE) received the B.Sc., M.Sc., and Lic. degrees in electrical and electromagnetic engineering from KTH, Royal Institute of Technology, Stockholm, Sweden, in 2016, 2019, and 2021, respectively. where, he is currently pursuing the Ph.D. degree in antennas and electromagnetics with the Division of Electromagnetic Engineering.

He has authored or coauthored over 70 peer-reviewed journal and conference papers. His research interests include transformation optics, lens antennas, periodic structures possessing higher symmetries and leaky wave antennas.

Mr. Oskar is also a member of the EurAAP working group for Early Careers in Antennas and Propagation (ECAP), where he is responsible for the ECAP mentoring program. He received the First Price in the Student Design Competition at APS/URSI 2016, the Best Student Paper Award at URSI Spain 2020, and the Best Antenna Technology Paper Award at EuCAP 2022 for his works.

Nelson J. G. Fonseca (Senior Member, IEEE) received the M.Eng. degree from the Ecole Nationale Supérieure d'Electrotechnique, Electronique, Informatique, Hydraulique et Télécommunications (ENSEEIHT), Toulouse, France, in 2003, the M.Sc. degree from the Ecole Polytechnique de Montreal, Montreal, QC, Canada, in 2003, and the Ph.D. degree from the Institut National Polytechnique de Toulouse, Université de Toulouse, Toulouse, in 2010, all in electrical engineering.

He is currently working as Innovation Manager for Anywaves, Toulouse, contributing to the development of their custom space-segment antennas portfolio. He is also the Founding Director of 3Space Innovation, Paris, France, a startup developing novel ground-segment and terrestrial wireless communication antenna systems. He has authored or coauthored more than 300 papers in peer-reviewed journals and conferences and has over 50 patents issued or pending. His research interests include multiple beam antennas for space missions, beamformer theory and design, ground terminal antennas, and novel manufacturing techniques.

Dr. Fonseca received several prizes and awards, including the Best Young Engineer Paper Award from the 29th ESA Workshop on Antennas in 2007, the ESA Teamwork Excellence Award in 2020, the Best Applied Technology Antenna Paper Award from EuCAP 2022, and the 2024 IEEE Journal of Microwaves Best Paper Award. He served as the TPC Co-Chair for the 18th European Conference on Antennas and Propagation (EuCAP2024) and is serving as the Vice-Chair for the 19th edition (EuCAP2025). He is currently serving as Associate Editor for IEEE TRANSACTIONS ON ANTENNAS AND PROPAGATION and *IET Microwaves, Antennas and Propagation* and a Topic Editor for IEEE JOURNAL OF MICROWAVES.

Oscar Quevedo-Teruel (Fellow, IEEE) received the Telecommunication Engineering and Ph.D. degrees from the Carlos III University of Madrid, Madrid, Spain, in 2005 and 2010, respectively.

From 2010 to 2011, he joined the Department of Theoretical Physics of Condensed Matter, Universidad Autonoma de Madrid, Madrid, as a Research Fellow, and went on to continue his post-doctoral research at the Queen Mary University of London, London, U.K., from 2011 to 2013. In 2014, he joined the Division of Electromagnetic Engineering and Fusion Science, School of Electrical Engineering and Computer Science, KTH Royal Institute of Technology, Stockholm, Sweden, where he is currently a Professor and the Director of the Master Program in Electromagnetics Fusion and Space Engineering. He has coauthored of more than 140 articles in international journals and more than 240 at international conferences. He has made scientific contributions to higher symmetries, transformation optics, lens antennas, metasurfaces, and high impedance surfaces.

Dr. Quevedo-Teruel has been a member of the European Association on Antennas and Propagation (EurAAP) Board of Directors since January 2021. Since January 2022, he has been the Vice-Chair for EurAAP. He was a Distinguished Lecturer of the IEEE Antennas and Propagation Society for the period of 2019–2022. He has been an Associate Editor of the IEEE TRANSACTIONS ON ANTENNAS AND PROPAGATION from 2018 to 2022 and a Track Editor since 2022.